Materials Science & Engineering A 777 (2020) 139081

Contents lists available at ScienceDirect

Materials Science & Engineering A

journal homepage: http://www.elsevier.com/locate/msea

Processing, multiscale microstructure refinement and mechanical property enhancement of hypoeutectic Al–Si alloys via in situ bimodal-sized TiB_2 particles

Qiang Li [a,b], Feng Qiu [a,b,d,*], Bai-Xin Dong [a,b], Xiang Gao [a,b], Shi-Li Shu [a,b], Hong-Yu Yang [c], Qi-Chuan Jiang [a,b,**]

[a] State Key Laboratory of Automotive Simulation and Control, Jilin University, PR China
[b] Key Laboratory of Automobile Materials, Ministry of Education and Department of Materials Science and Engineering, Jilin University, Renmin Street NO. 5988, Changchun, Jilin Province, 130025, PR China
[c] School of Materials Science and Engineering, Jiangsu University of Science and Technology, Zhenjiang, 212003, Jiangsu, China
[d] Qingdao Automotive Research Institute of Jilin University, PR China

ARTICLE INFO

Keywords:
In situ bimodal-sized TiB_2 particles
Hypoeutectic Al–Si alloys
Multiscale refinement
Strengthening mechanisms

ABSTRACT

A comprehensive investigation of the trace additions of in situ novel bimodal-sized (nano and submicron) TiB_2 particles on the solidification behavior, microstructure and mechanical property evolution of Al–7Si–4Cu alloys were carried out through remelting and dilution-assisted ultrasonic vibration. The results showed that both the primary α-Al dendrites and eutectic Si structure were greatly refined in the presence of 0.7 wt% bimodal-sized TiB_2 particles, with a reduction of 79.0% and 53.7% compared to the base alloy, which is far beyond the efficiency of micron-sized TiB_2 particles. Additionally, the average diameter of the θ' precipitates was greatly reduced by 32.7%. Thermal analysis revealed that the bimodal-sized TiB_2 particles sharply shifted the nucleation temperature of primary α-Al from 600.7 °C to 607.1 °C; meanwhile, the corresponding recalescence undercooling decreased by 3.6 °C. More importantly, in contrast with the common dilemma of strength-ductility trade-off, the yield strength and elongation to fracture of the inoculated Al–7Si–4Cu alloy were simultaneously and significantly improved by 26.3% and 71.1%, respectively. In this work, the mechanisms of multiscale microstructure refinement and mechanical property enhancement by bimodal-sized TiB_2 particles were systematically discussed.

1. Introduction

Hypoeutectic Al–Si alloys, which are primarily characterized by a unique combination of low density, good formability, high thermodynamic stability, low coefficient of expansion and excellent wear resistance, have been investigated extensively and are recognized as ideal candidates for automotive components [1–4]. However, it is also well documented that their strength and ductility still cannot meet the increasingly high requirements of some crucial structural parts due to the coarse α-Al dendrites and brittle and flaky eutectic Si phase that aggregates in the interdendritic regions [1,5].

To improve the mechanical properties of this metallic material, precipitates are often induced in the interior of the matrix to disrupt the dislocations in terms of precipitation strengthening, whereby the spatially dispersive nanosized θ' precipitates, via the addition of the elemental Cu accompanied by a subsequent T6 heat treatment, are supposed to be the highly efficient strengthening phases [6], but the ductility may be somewhat sacrificed [7]. Additionally, Sr [8], Ce [9] and La [10] elements could effectively modify the flake-like eutectic Si into a fibrous morphology and then improve the ductility of the Al–Si alloys, but it seems that their effects on the primary α-Al are limited; thus, the strength of these alloys increases only marginally. Furthermore, other modifiers, such as Al-Sc [11,12] for primary α-Al and eutectic Si modification, contain expensive rare earth elements and are

* Corresponding author. Key Laboratory of Automobile Materials, Ministry of Education and Department of Materials Science and Engineering, Jilin University, Renmin Street NO. 5988, Changchun, Jilin Province, 130025, PR China.
** Corresponding author. Key Laboratory of Automobile Materials, Ministry of Education and Department of Materials Science and Engineering, Jilin University, Renmin Street NO. 5988, Changchun, Jilin Province, 130025, PR China.
E-mail addresses: qiufeng@jlu.edu.cn (F. Qiu), jqc@jlu.edu.cn (Q.-C. Jiang).

https://doi.org/10.1016/j.msea.2020.139081
Received 16 June 2019; Received in revised form 4 February 2020; Accepted 7 February 2020
Available online 8 February 2020

not commercially available for mass production due to their high cost. Actually, adding grain-refining particles as inoculants, accompanied by ultrasonic vibration, during the solidification of Al alloys is extensively recognized as the most effective and simplest method by which to promote a reproducible, sound, uniform and refined equiaxed grain structure, which then facilitates the improvement in both the strength and ductility of the alloy [13,14]. Normally, the standard grain-refining practice for industrial manufacturing is to introduce super-stoichiometric Al–Ti–B (e.g., Al-5wt%Ti-1wt%B, hereafter in weight percentage) master alloys, which usually contain micron-sized TiB2 and Al3Ti particles, into the molten Al [15,16]. It is widely accepted that the acquired efficient grain refining is attributed to the potential heterogeneous nucleation sites that are provided by the TiB_2 particles and the strong growth restriction effects of the solute Ti (dissolved from Al_3Ti) for the α-Al crystals [16–18]. Nevertheless, the elemental Si in Al–Si alloys (when the Si content exceeds 3%) is likely to react with Ti and form Ti–Si compounds, which seriously degrade their nucleation, i.e., poisoning effects occur [19]. Moreover, the refinement of the second phases by the Al–5Ti–1B master alloy is even negligible, which therefore determines the marginal improvement in the mechanical properties. Similar results also occur for commonly used Al–Ti–C master alloys because both TiC and Al_3Ti particles are unstable in Al–Si alloys and are very likely to react with Si [20]. Recently, Al–TiB_2 master alloys containing only in situ TiB_2 particles have been shown to possess high chemical stability and grain-refining potency in Al–Si alloys [21–23]. The most popular method to prepare potent in situ TiB_2 particles is through the chemical reaction in the Al–K_2TiF_6–KBF_4 system, but most of the particles are micron in size, which results in a lower grain-refining efficiency when compared with that of their nanosized counterparts. Moreover, alloys with micron-sized particle addition commonly undergo a strength-ductility trade-off [24–26]. Therefore, considerable research has been carried out to simultaneously achieve high strength and ductility by reducing the particle size from the traditional micron-scale to the nanoscale [27–30].

More recently, innovative bimodal-sized particles, mainly a mixture of nano- and micron-sized particles, have been recognized as novel grain refiners. It has been recently suggested that they exhibit superior performance to those counterparts with single-sized particles [31,32]. In this regard, this approach may be expected to be a novel strategy for synergistically enhancing the strength and ductility of metallic material by adding a mixture of nanosized TiB_2 particles and certain amounts of submicron-sized TiB_2 particles. Nevertheless, to the best of our knowledge, the underlying reason for this response has not been fully understood. In comparison with well-reported single-sized reinforcements, there is little research on Al alloys that have been inoculated by in situ bimodal-sized TiB_2 particles, particularly Al–Si alloys.

In our work, the correlation between the microstructure and mechanical properties of the Al–7Si–4Cu alloys inoculated by in situ bimodal-sized TiB_2 particles was well established. Furthermore, the mechanisms controlling size and morphology of the primary α-Al dendrites, eutectic Si and θ' precipitates and the mechanical properties of the inoculated alloys were systematically analyzed and discussed. This work may be a remarkable contribution to further scientific research and practical applications.

2. Material design and fabrication

In our work, two steps were involved in the experimental procedure: synthesis of Al–TiB_2 master alloys, and remelting and dilution-assisted ultrasonic vibration. The relevant experimental set-ups and procedures are schematically illustrated in Fig. 1.

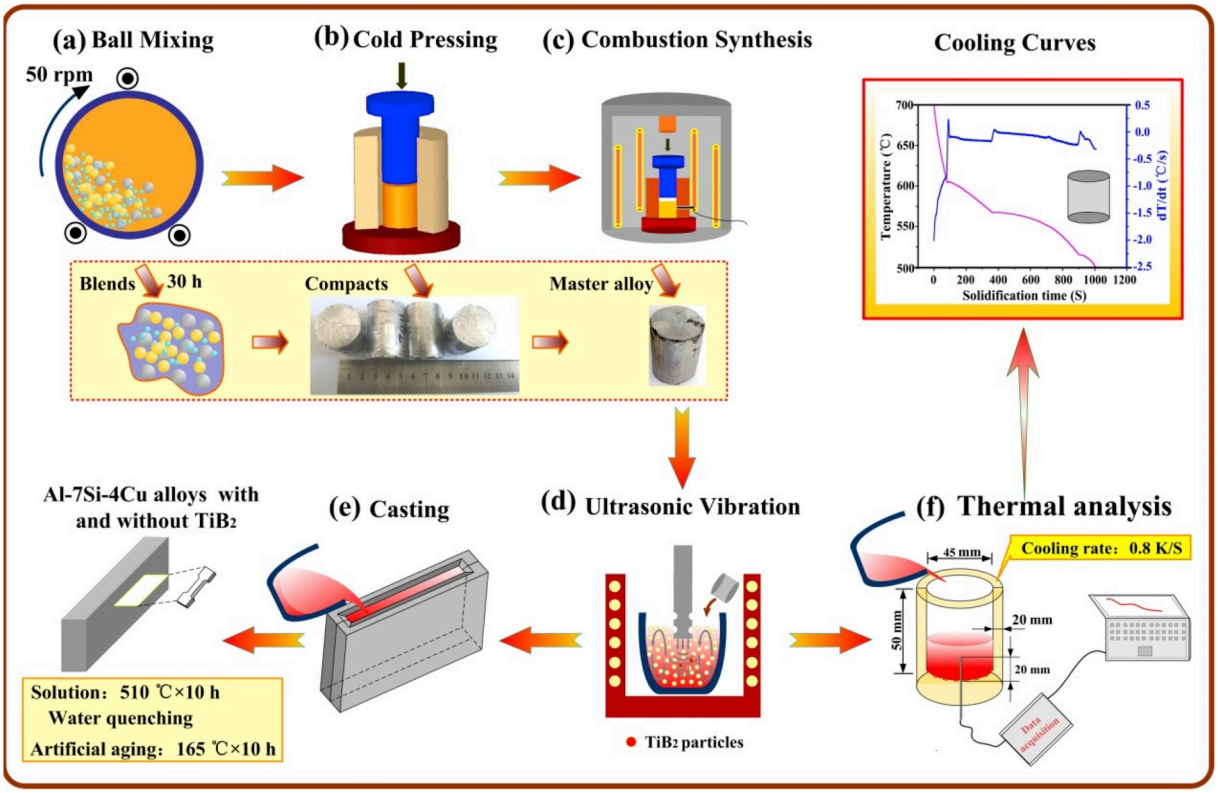

Fig. 1. Fabrication processing of Al–7Si–4Cu alloys inoculated by bimodal-sized TiB_2 particles assisted by ultrasonic vibration. (a) Mixture of Al powders, Ti powders and B powders by ball mixing; (b) condensing the blends into a cylindrical compact; (c) the synthesis process of Al–TiB_2 master alloys; (d) remelting and dilution-assisted ultrasonic vibration; (e) pouring the melts at 750 °C; (f) cooling curve measurement with a refractory brick mold.

2.1. Synthesis of Al–TiB_2 master alloy

The preparation of the Al–20%TiB_2 and Al–50%TiB_2 master alloys included three steps: First, the three reactants, Al powder (99.5% purity, ~48 μm), Ti powder (99.5% purity, ~25 μm) and B powder (99.5% purity, ~100 nm), were initially mixed uniformly using a ball mixing machine at 50 rpm for 30 h (see Fig. 1 (a)). Second, the blends were wrapped in rod-shaped Al foils and were consolidated into a cylindrical compact with dimensions of Φ30×40 mm under axial stress of approximately 60 kN for 15 s (see Fig. 1(b)). Finally, the compact was placed inside a vacuum sintering furnace with a heating rate of 30 °C/min (see Fig. 1 (c)). The graphite electrode rods inside the vacuum furnace worked as the heating source. As the temperature was mutated, a large amount of TiB_2 particles were synthesized and this process lasted less than 5 s.

2.2. Remelting and dilution-assisted ultrasonic vibration

First, the as-received Al–7Si–4Cu alloys were remelted in a clay-bonded graphite crucible using a resistance furnace at 850 °C. Prior to the addition, the Al–20TiB_2 master alloy was initially preheated in another resistance furnace and held isothermally at 550 °C for 2 h. Then, according to the addition levels of 0.1%, 0.3%, 0.7% and 1.0% TiB_2 particles, the Al–20TiB_2 master alloy was fed into the Al–7Si–4Cu melts and was stirred sufficiently using a graphite rod for almost 3 min. Afterward, the preheated niobium probe of the ultrasonic was immersed into the molten Al, about 25 mm below the melt surface, to further disperse the small-sized TiB_2 particles under a frequency of 19.9 kHz for approximately 5 min, and then the probe was lifted out quickly. Subsequently, after slag removing and degassing, the melts were cast at 750 °C into the permanent mold (preheated up to 100 °C) with dimensions of 200 × 20×150 mm^3, as shown in Fig. 1 (d and e). The alloys with Al–20TiB_2 master alloy addition were denoted as BS-0.0, BS-0.1, BS-0.3 BS-0.7 and BS-1.0. For comparison, Al–50TiB_2 master alloy was also added at an addition level of 0.7% TiB_2 particles, and the obtained alloy was referred to as MS-0.7. To maintain consistent experimental conditions, ultrasonic treatment was also conducted during the preparation of the Al–7Si–4Cu alloy without TiB_2 particle addition. The chemical compositions of the fabricated Al–7Si–4Cu alloys are shown in Table 1.

2.3. Thermal analysis

To precisely determine the influence of bimodal-sized TiB_2 particles on the thermal kinetics of the melts during cooling, the solidification behavior analysis of the Al–7Si–4Cu alloys with and without TiB_2 particle addition was conducted using a refractory brick mold (inner cavity dimensions: Φ45×50 mm; wall thickness: 20 mm) with a K-type thermocouple (tip at approximately 20 mm from the bottom of the mold) connected to the data acquisition system (see Fig. 1 (f)). The cooling rate of the brick mold was as low as 0.8 °C/s. The pouring temperature of the melts was also set at 750 °C, and a frequency of 40 Hz was used during the measurement. The characteristic temperatures were obtained through a careful comparison of the obtained cooling curves and their corresponding first derivatives and second derivatives, according to Ref. [33]. For convenience, the first noticeable transformation of temperature, in terms of the derivative, was the nucleation point, which was defined as T_N. Furthermore, the minimum and maximum temperatures in the cooling curves during recalescence were defined as T_{Min} and T_G, respectively, and the recalescence undercoolings ($\Delta T_{\alpha\text{-}Al}$ and $\Delta T_{Al\text{-}Si}$) of the primary α-Al and eutectic Al–Si reactions were taken as the difference between their T_{Min} and T_G values, respectively.

Table 1
The chemical compositions of the fabricated Al–7Si–4Cu alloys (wt%).

Alloy	Element content						
	Si	Cu	Fe	V	Ni	Zn	Al
BS-0.0	6.80	4.02	0.11	0.02	0.010	0.010	Balance
BS-0.1	6.91	3.90	0.10	0.007	0.010	0.020	Balance
BS-0.3	6.72	4.06	0.09	0.01	0.002	0.008	Balance
BS-0.7	6.85	3.86	0.12	0.02	0.030	0.020	Balance
BS-1.0	6.95	4.05	0.11	0.02	0.006	0.009	Balance
MS-0.7	7.01	3.95	0.11	0.01	0.005	0.005	Balance

2.4. Characterization

The fabricated Al–20TiB_2 master alloy was characterized by X-ray diffraction (XRD) equipment (Moldel D/Max 2500PC Rigaku, Japan) to determine the phase constituents, and then the in situ TiB_2 particles were extracted with a 10 vol% hydrochloric acid solution. Field emission scanning electron microscopy (FESEM, JSM-6700F, Japan) was used to analyze the three-dimensional morphology of TiB_2 particles. Solution treatment at 510 °C for 10 h, water quenching treatment and artificial aging treatment at 165 °C for 10 h were successively applied to the solidified Al–7Si–4Cu samples with and without TiB_2 addition. Then, both the as-cast and heat-treated samples were mechanically ground, polished and finally etched with 5 vol% HBF_4 solution. Afterward, optical microscopy (OM, Olympus PMG3, Japan), scanning electron microscopy (SEM, Tescan vega3 XM, Czech Republic) equipped with an energy dispersive spectrometer (EDS), and high-resolution transmission electron microscopy (HRTEM, JEM-2100F, Japan) were used to characterize the microstructural evolution of the alloys. The size distributions of the TiB_2 particles, α-Al grains, eutectic Si, and θ' precipitate were measured from the FESEM images, OM images, SEM images, and HRTEM images, respectively, using Nano Measurer software 1.2 [14]. For accuracy, more than 10 images were selected stochastically and analyzed for each phase to obtain the average value. Tensile tests of the heat-treated samples were carried out with a cross-section of 4.0×2.5 mm^2 and a gauge length of 10.0 mm using servo-hydraulic materials testing equipment (MTS, MTS 810, USA).

3. Results

3.1. Microstructural analysis of the synthetic Al–TiB_2 master alloy

As exhibited by the XRD spectrum in Fig. 2 (a), only the TiB_2 and α-Al phases could be detected in both the Al–20%TiB_2 and Al–50%TiB_2 master alloy, while no brittle Al_3Ti compounds were discernable, which indicates that the reaction process proceeded completely. The TiB_2 particles in the Al–20%TiB_2 master alloy are shown in Fig. 2 (b). It is interesting to find that the in situ TiB_2 particles could be clearly divided into nano- and submicron-sized particles, as indicated by the dash-dotted lines. The submicron-sized particles mainly exhibited typical hexagonal prism shapes, while most of the nanosized particles presented a spheroidal morphology, which may be due to their incomplete growth. In addition, the TiB_2 particles were isolated and were not clustered throughout the microstructure, which was highly beneficial for further dispersion during the melting process. To further demonstrate the size distribution and morphology of the as-fabricated bimodal-sized TiB_2 particles, the TiB_2 particles were extracted and characterized by FESEM, as shown in Fig. 2 (c). According to the statistical histograms in Fig. 2 (d), the size distribution of the TiB_2 particles in the Al–20%TiB_2 master alloy ranged from less than 100 nm–350 nm. In contrast, as shown in Fig. 2 (e and f), the TiB_2 particles in the Al–50%TiB_2 master alloy exhibited the similar morphology to those in the Al–20%TiB_2 master alloy but were much larger, with an average particle size of 0.73 μm.

3.2. Phase analysis of the Al–7Si–4Cu alloy

The as-solidified microstructures and characteristic phases of the Al–7Si–4Cu alloy are clearly exhibited in Fig. 3. As observed from the OM micrograph in Fig. 3 (a), coarse primary α-Al dendrites and eutectic

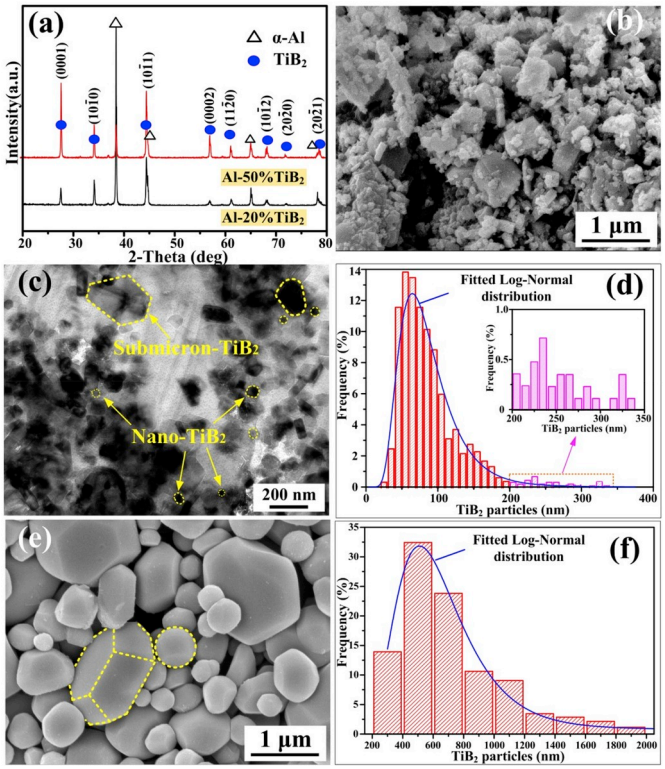

Fig. 2. (a) XRD spectra of the Al–20%TiB_2 and Al–50%TiB_2 master alloys; (b) TEM micrograph of Al–20%TiB_2 master alloy; (c) FESEM micrograph of the extracted TiB_2 particles; (d) statistical analysis of TiB_2 particle sizes in the Al–20%TiB_2 master alloy; (e) FESEM micrograph of the extracted TiB_2 particles; and (f) statistical analysis of TiB_2 particle sizes in the Al–50%TiB_2 master alloy.

phases in the interdendritic regions were present in the typical microstructure of the Al–7Si–4Cu alloy. The backscattered electron (BSE) magnification micrographs in Fig. 3 (b and c) and the element mapping analysis spectra in Fig. 3(d–f) suggest that the eutectic phases were mainly composed of gray flake-like eutectic Si structures with needle- or plate-like morphologies and bright, large Al_2Cu phases. Moreover, the Al_2Cu intermetallic structures were interconnected with the eutectic Si in the interdendritic regions.

3.3. Microstructures of the inoculated Al–7Si–4Cu alloys

The grain-refining response of Al–7Si–4Cu alloys to the added in situ bimodal-sized and micron-sized TiB_2 particles is clearly shown in the polarized optical micrographs in Fig. 4(a–f). Obviously, the Al–7Si–4Cu alloy without TiB_2 addition presented a coarse and uneven dendrite structure, with an average grain size of up to 1150 μm. As shown in Fig. 4(b–e), the bimodal-sized TiB_2 particles exhibited continuous and substantial grain refinement effects on the microstructures of Al–7Si–4Cu alloys with increasing addition levels. Upon minor addition of 0.1% bimodal-sized TiB_2 particles, the coarse dendrites were significantly refined, with an average size of 367 μm. With a further increase in TiB_2 particles, the morphology of α-Al gradually transformed into fine and equiaxed dendrites. At 0.7% bimodal-sized TiB_2 particle addition, the grain size sharply decreased to 241 μm, a reduction of 79.0%. As the addition level of bimodal-sized TiB_2 particles increased to 1.0%, the grain size was further reduced by 85.7%. Comparatively, as shown in Fig. 4 (f), although 0.7% of the micron-sized TiB_2 particles could refine the grain size of the Al–7Si–4Cu alloy to 507 μm, the grain-refining efficacy was visibly inferior to that of the bimodal-sized TiB_2 particles.

The size and morphologies of the eutectic Si in the Al–7Si–4Cu alloys with and without TiB_2 particle addition in the as-cast state are clearly shown in the BSE micrographs in Fig. 5(a–f), and the detailed statistics of their lengths are illustrated in Fig. 5(m–r). The eutectic Si phase occurred as coarse and long structures, with an average size of 18.8 μm in the base alloy. Comparatively, the eutectic Si was well refined by the bimodal-sized TiB_2 particles and gradually transformed from long needle-shaped structures to short structures with increasing addition levels. In particular, at 0.7% bimodal-sized TiB_2 particle addition, the size of the eutectic Si was greatly reduced to 8.7 μm, a reduction of up to 53.7%. In contrast, the micron-sized TiB_2 could not substantially transform the size and morphology of the eutectic Si structure. It is well known that the solution treatment could also transform the size and morphology of the eutectic Si structure. Fig. 5(g–l) shows that the eutectic Si exhibited a much shorter structure or even a globular shape after heat treatment. Combined with the statistical graphs in Fig. 5(s–x), a significant refinement of the as-cast eutectic Si induced by the bimodal-sized TiB_2 particles was still observed after heat treatment. Specifically, with a 0.7% addition level, the size of the eutectic Si

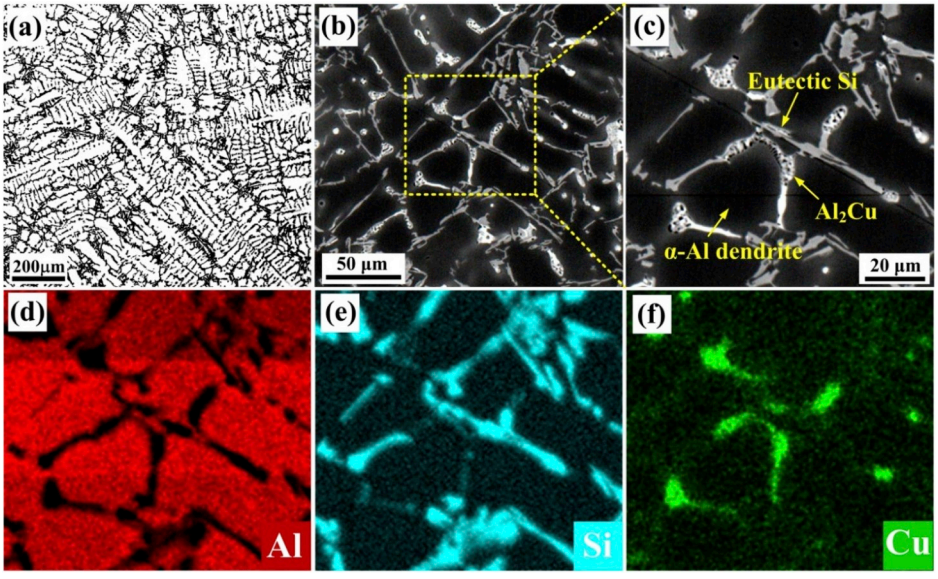

Fig. 3. (a) OM micrograph and (b–c) BSE micrographs showing the representative phase compositions in the as-cast base alloy and the corresponding EDS maps of (d) Al; (e) Si and (f) Cu.

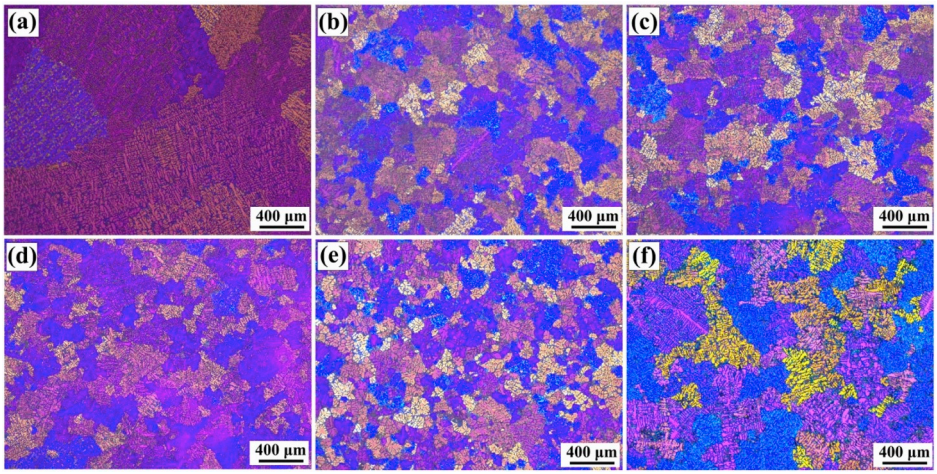

Fig. 4. The polarized optical micrographs of the as-cast Al–7Si–4Cu inoculated by various addition levels of TiB_2 particles: (a) BS-0.0; (b) BS-0.1; (c) BS-0.3; (d) BS-0.7; (e) BS-1.0 and (f) MS-0.7.

decreased from 10.9 μm to 6.3 μm, with a reduction of 42.2%.

In Cu-containing aluminum alloys, metastable precipitate phases are formed from the decomposition of a supersaturated solid solution during the precipitation process. The sequence of steps for the Al–Cu precipitation process is Al_{ss}→ Guinier Preston (GP I zones)→ θ'' (GP II zones)→ θ' →θ [34]. θ' precipitate, a metastable phase with the stoichiometry of Al_2Cu, is the dominant strengthening phase at the peak aging condition and exhibits a high-aspect-ratio plate-like morphology with coherent interfaces $(001)_{\theta'}\|(001)_{Al}$ parallel to their broad faces. At approximately 250 °C, θ' precipitate transforms to the thermodynamically stable θ phase, which is incoherent with the Al matrix and results in decreasing mechanical properties [34]. Fig. 6 shows the diameter and morphology of θ' precipitates in the Al–7Si–4Cu alloys without and with bimodal-sized TiB_2 addition after artificial aging at 165 °C for 10 h. As shown in Fig. 6 (a, b and c), the coarse θ' precipitates in the base alloy were greatly refined and the density was also enhanced with the addition of bimodal-sized TiB_2 particles. According to the statistical results, the average diameter of θ' was reduced from 52±6.2 nm to 42± 3.5 nm with addition of 0.1% bimodal-sized TiB_2 particles. When 0.7% bimodal-sized TiB_2 particles were added, the average diameter of θ' further decreased to 35±3.2 nm, a decrease of 32.7%. Moreover, the average thickness also decreased from 3.7±0.3 nm to 3.2± 0.2 and nm 2.8±0.2 nm, respectively. Furthermore, the θ' precipitates were distributed much more uniformly throughout the microstructure compared with those of the base alloy. The HRTEM micrograph and SAED pattern of area D in Fig. (c) were further shown in Fig. 6 (d) and (e), respectively. As observed, the interface between the θ' precipitate and the α-Al matrix was identified to be very coherent, which was highly beneficial for the improvement in the strength.

3.4. Tensile properties and fracture behavior

Fig. 7(a) shows the engineering stress-strain curves of the Al–7Si–4Cu alloys inoculated with various addition levels of TiB_2 particles, along with the detailed statistical data given in Table 2. Overall, the yield strength ($\sigma_{0.2}$), ultimate tensile strength (σ_b) and elongation to fracture (ε_f) of the inoculated alloys were improved simultaneously when compared to those of the base alloy. Upon the addition of 0.1% bimodal-sized TiB_2 particles, $\sigma_{0.2}$, σ_b, and ε_f were enhanced to 273 MPa, 398 MPa and 9.8%, significantly improved by 17.7%, 11.5% and 28.9%, respectively, relative to the low $\sigma_{0.2}$ (232 MPa), σ_b (357 MPa), and ε_f (7.6%) values of the base alloy. This improving tendency continued until the 0.7% bimodal-sized TiB_2 addition level. At this level, $\sigma_{0.2}$, σ_b, and ε_f were significantly enhanced to 293 MPa, 419 MPa and 13.0%, which were 26.3%, 17.4% and 71.1% higher than those of the base alloy. However, with 1.0% bimodal-sized TiB_2 particle addition, the mechanical properties were severely deteriorated. As shown in the SEM photograph in Fig. 7 (b), serious aggregations of the added bimodal-sized TiB_2 particles formed at the interdendritic regions, as confirmed by the corresponding EDS elemental distribution maps in Fig. 7(c–f). In contrast, $\sigma_{0.2}$, σ_b and ε_f of the Al–7Si–4Cu alloy with a 0.7% micron-sized TiB_2 particle addition were enhanced by only 16.4%, 3.6% and 14.5%, respectively. Therefore, the bimodal-sized TiB_2 particles exhibited a much higher strengthening and toughening efficiency.

Fig. 8(a–e) shows the fracture morphology of the base alloy and alloys with various TiB_2 particle additions. As seen clearly, the Al–7Si–4Cu alloy exhibited evident irregular cleavage planes and few dimples, which were closely related to the blocky eutectic Si and the coarse α-Al dendrites. As shown in Fig. 8(f–i), the large and brittle eutectic Si in the base alloy, as the main source of stress concentration and thus crack propagation, led to the formation of an intergranular fracture under a load. However, smaller dimples were uniformly distributed in the Al–7Si–4Cu alloys with increasing the bimodal-sized TiB_2 addition levels. In contrast, as shown in Fig. 8 (e), the alloy with micron-sized TiB_2 particle addition exhibited much fewer and larger dimples than those alloys with bimodal-sized TiB_2 addition, which also suggested that the latter underwent more serious plastic deformation prior to fracture; thus, higher strength and elongation were obtained.

4. Discussion

4.1. Microstructure refinement analysis

As shown in the typical cooling curves (500–700 °C) in Fig. 9 (a), three main plateaus were successively involved during the solidification processing of the Al–7Si–4Cu melts with or without the addition of bimodal-sized TiB_2 particles, which corresponded to the primary α-Al, eutectic Al–Si reaction, and eutectic Al_2Cu reaction, respectively [35]. The relevant data, as summarized in Table 3, were derived from the cooling curves and their corresponding first (dT/dt) and second (d^2T/dt^2) derivatives in Fig. 9(d–e). The critical nucleation temperature of the base alloy was determined to be 600.7 °C. In contrast, the new α-Al crystals were initiated and shifted upward at 607.1 °C in the presence of 0.7% bimodal-sized TiB_2 particles. Furthermore, as clearly shown in Fig. 9 (b), the recalescence undercooling (ΔT) of the primary α-Al was reduced by 3.7 °C by the bimodal-sized TiB_2 particles. All the above observations strongly indicated that the added bimodal-sized TiB_2 particles were highly potent at promoting the heterogeneous nucleation of α-Al crystals at a lower undercooling [36]. As the solidification progressed, an Al–Si eutectic reaction occurred. The recalescence

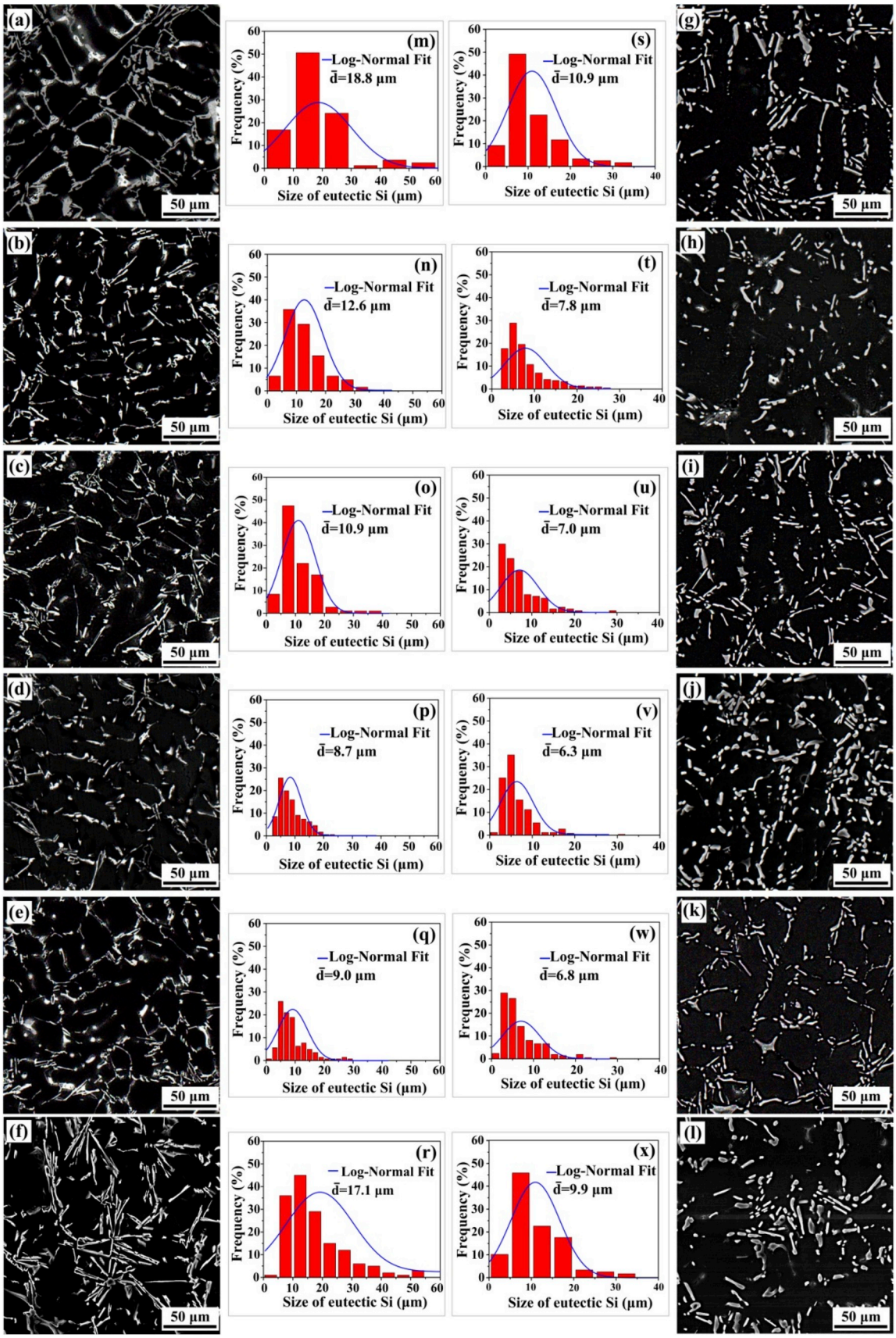

Fig. 5. BSE micrographs showing the size and morphologies of the eutectic Si structure under the as-cast condition with the corresponding size statistics: (a, m) BS-0.0; (b, n) BS-0.1; (c, o) BS-0.3; (d, p) BS-0.7; (e, q) BS-1.0; and (f, r) MS-0.7. Additional BSE micrographs showing the size and morphologies of the eutectic Si structure under heat treatment condition with the corresponding size statistics: (g, s) BS-0.0; (h, t) BS-0.1; (i, u) BS-0.3; (j, v) BS-0.7 and (k, w) BS-1.0; and (i, x) MS-0.7.

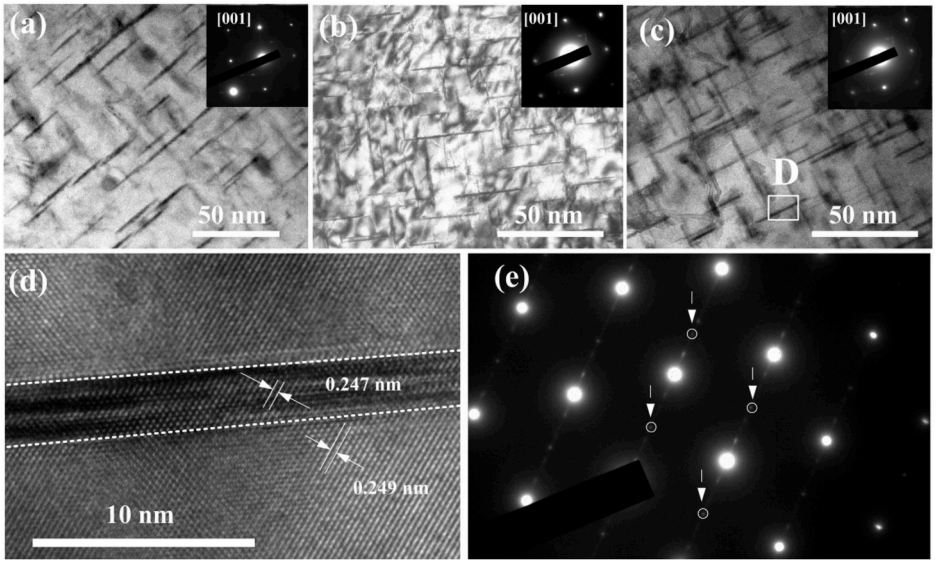

Fig. 6. TEM micrographs taken in the $[001]_{Al}$ zone axis showing the diameter and morphologies of the θ' precipitates in (a) BS-0.0, (b) BS-0.1 and (c) BS-0.7. (d) and (e) show the HRTEM micrograph and selected area electron diffraction (SAED) pattern of area D in Fig. (c), respectively.

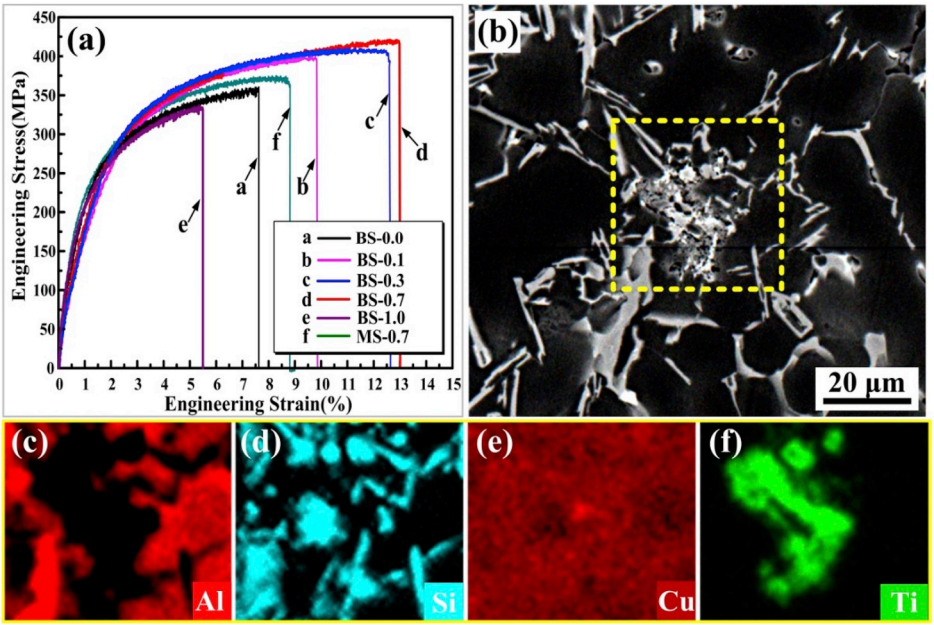

Fig. 7. (a) Engineering stress-strain curves of the Al–7Si–4Cu alloys with various addition levels of TiB_2 particles; (b) SEM photograph showing the area with severe aggregation in BS-1.0 and the corresponding EDS elemental distribution maps of (c) Al; (d) Si; (e) Cu and (f) Ti.

Table 2
Engineering stress-strain curves of the Al–7Si–4Cu alloys with various addition levels of TiB_2 particles.

Alloy	$\sigma_{0.2}$(MPa)	σ_b(MPa)	ε_f(%)
BS-0.0	232 ± 4	357 ± 10	7.6 ± 1.0
BS-0.1	273 ± 6	398 ± 12	9.8 ± 1.2
BS-0.3	286 ± 6	409 ± 11	12.6 ± 1.2
BS-0.7	293 ± 8	419 ± 13	13.0 ± 1.4
BS-1.0	225 ± 5	337 ± 13	5.5 ± 1.6
MS-0.7	270 ± 4	370 ± 14	8.7 ± 1.3

undercoolings of the Al–Si eutectic for the alloys without and with 0.7% TiB_2 particles were measured with a negligible difference, which were 0.6 °C and 0.4 °C, respectively. However, the nucleation temperature and the growth temperature of the Al–Si eutectic decreased by 1.1 °C and 1.2 °C, respectively, which is a typical characteristic of eutectic Si refinement [4].

It is well accepted that the heterogeneous nucleation potency of nucleant particles is highly dependent on their crystallographic matching relationship with α-Al (typically <10%), which represents interfacial energy [37,38]. Fan [39] suggested that the added ex situ TiB_2 particles could not effectively refine the microstructure of commercial pure Al. Other researchers have also noted that an Al_3Ti layer formed from the excess Ti is required to trigger the TiB_2 particles as the active nucleating particles [39–41]. Moreover, according to the edge-to-edge matching model developed by Zhang et al. [37], there exist only 2 crystallographic orientation relationships (ORs) between the TiB_2 and α-Al phases, i.e., $(200)_{Al}\|(10\bar{1}1)_{TiB2}$, $[011]_{Al}\|[1\bar{2}10]_{TiB2}$ and $(200)_{Al}\|(11\bar{2}0)_{TiB2}$, $[\bar{1}12]_{Al}\|[1\bar{1}00]_{TiB2}$. In contrast, Al_3Ti and α-Al phases have 4 ORs, i.e.,

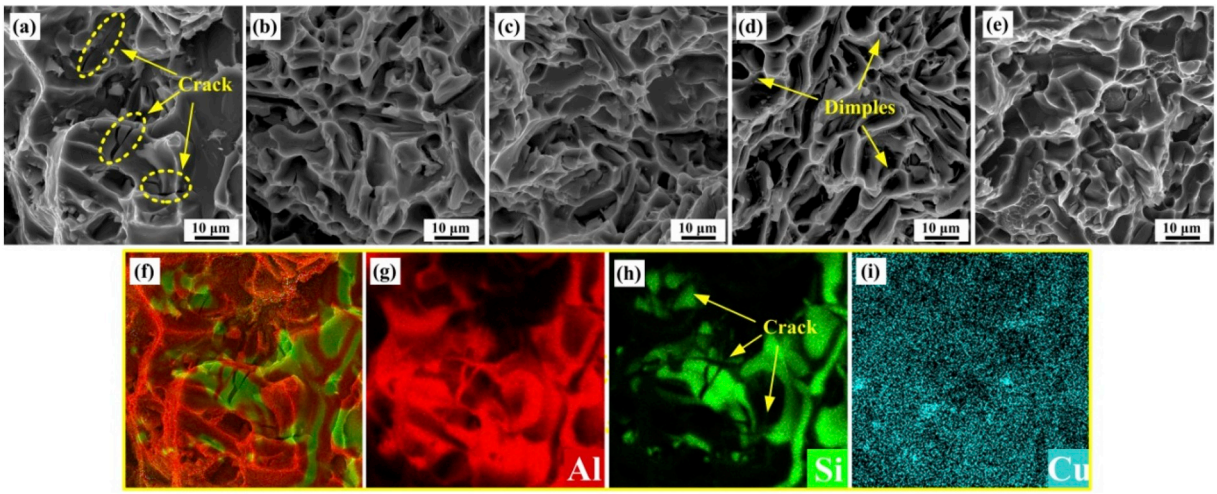

Fig. 8. Fracture surface morphologies: (a) BS-0.0; (b) BS-0.1; (c) BS-0.3; (d) BS-0.7 and (d) MS-0.7. Corresponding EDS elemental distribution maps of (e) via a layered graphic of (f) Al; (g) Si and (h) Cu elements in the BS-0.0.

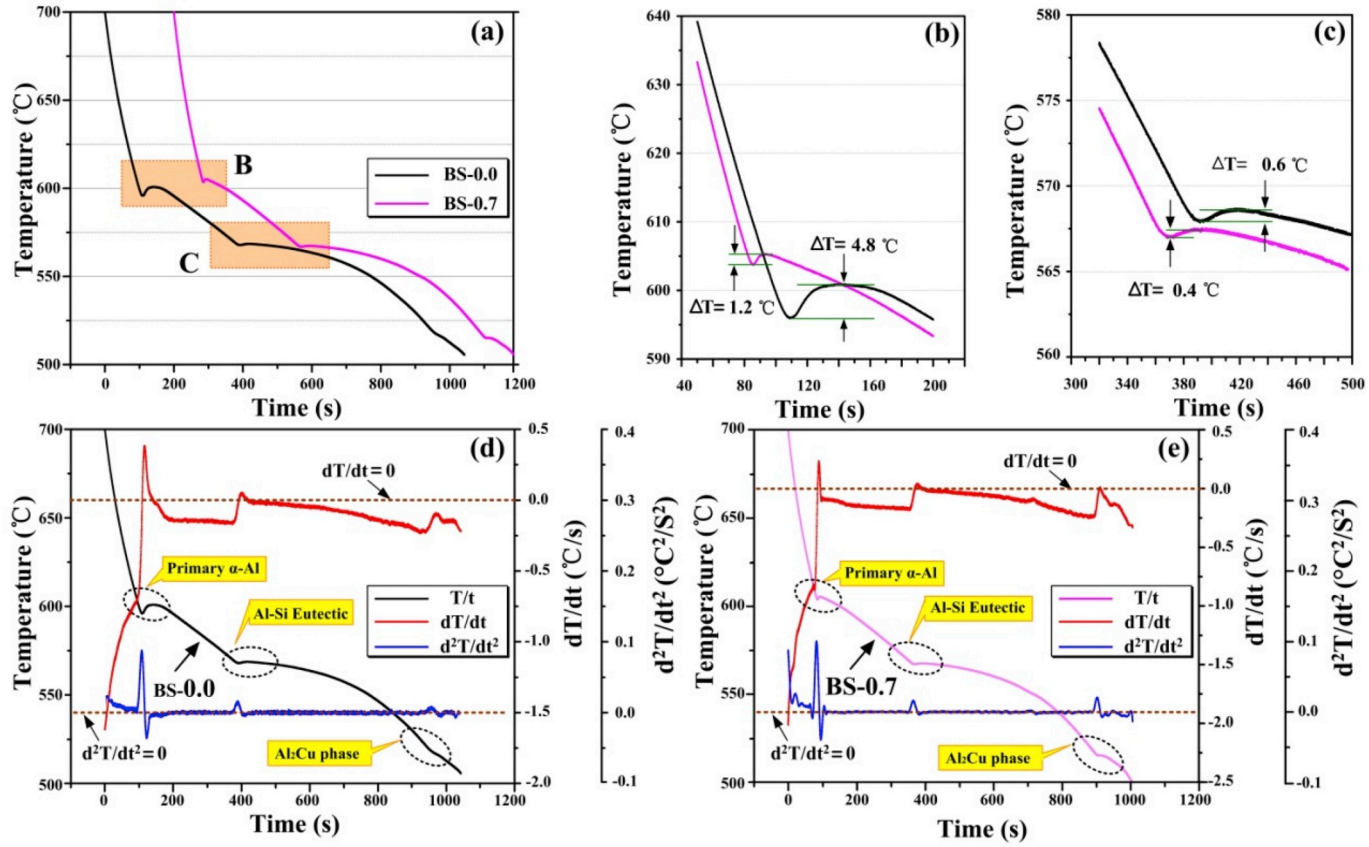

Fig. 9. The cooling curves of the as-fabricated Al–7Si–4Cu melts. (a) Cooling curves of BS-0.0 and BS-0.7; (b) magnification of the shadowed area B in (a); and (c) magnification of the shadowed area C in (a). (d) The cooling curve of BS-0.0 and the corresponding first (dT/dt) and second (d^2T/dt^2) derivatives; (e) the cooling curve of BS-0.7 and the corresponding first (dT/dt) and second (d^2T/dt^2) derivatives.

Table 3
Characteristic temperature (°C) statistical data of the as-fabricated Al–Si–Cu melts with and without the addition of TiB_2 particles during cooling.

Alloy	Primary α-Al				Eutectic Al–Si			
	$T_{N,\alpha\text{-Al}}$	$T_{M,\alpha\text{-Al}}$	$T_{G,\alpha\text{-Al}}$	$\Delta T_{\alpha\text{-Al}}$	$T_{N,\ Al-Si}$	$T_{M,Al-Si}$	$T_{G,Al-Si}$	$\Delta T_{Al\text{-}Si}$
BS-0.0	600.7	596.1	600.9	4.8	569.5	568.1	568.7	0.6
BS-0.7	607.1	604.2	605.4	1.2	568.4	567.1	567.5	0.4

$(111)_{Al}\|(112)_{Al3Ti}$, $[1\bar{1}0]_{Al}\|[20\bar{1}]_{Al3Ti}$; $(111)_{Al}\|(112)_{Al3Ti}$, $[1\bar{1}0]_{Al}\|[\bar{1}10]_{Al3Ti}$; $(200)_{Al}\|(200)_{Al3Ti}$, $[011]_{Al}\|[021]_{Al3Ti}$ and $(200)_{Al}\|(200)_{Al3Ti}$, $[010]_{Al}\|[010]_{Al3Ti}$. Additionally, the Al_3Ti and α-Al phases show smaller interatomic spacing misfits and the interplanar spacing mismatches, which indicates that Al_3Ti is more powerful than TiB_2 as a grain refiner. Therefore, it is speculated that the TiB_2 particles, with a monolayer of Al_3Ti on their surface, acted as the heterogeneous nucleating substrates for primary α-Al. In addition, according to the free growth model proposed by Greer and coworkers [42], the size distribution of the nucleant particles is another important factor and plays a crucial role in determining the resultant grain refinement in terms of thermodynamics, which could be quantitatively related to the critical undercooling, as follows:

$$\Delta T_{fg} = \frac{4\gamma}{\Delta S_v d} \tag{1}$$

where ΔT_{fg} is the critical undercooling required for the free growth of α-Al crystals; γ is the interfacial energy between the melt and the nucleating particles; ΔS_v is the entropy of fusion per unit volume; and d is the diameter of the particles.

For a given particle, the critical undercooling for free growth is also quantitatively determined. Accordingly, the new crystals will be preferentially initiated by the larger particles in terms of the thermodynamic driving force, while the smaller ones may be completely suppressed due to the released latent heat from the growing nucleated grains.

Fig. 10 (a) shows the schematic illustration of the effects of bimodal-sized TiB_2 particles during solidification. In our work, in contrast with the nanosized particles, the submicron-sized TiB_2 particles were more energetically favorable for providing heterogeneous nucleation sites for α-Al crystals. However, only trace amounts of approximately 1.0% of the TiB_2 particles were reported to have the opportunity to be activated for the nucleation of α-Al grains [42]. Once the steady crystal formed, the S/L interface advanced radially and started to grow toward the surrounding melt. Furthermore, the dispersed TiB_2 particles in the melts by ultrasonic vibration underwent redistribution during solidification. A large proportion of the TiB_2 particles, especially the nanosized particles, were driven to assemble onto the S/L interface by the reduction of surface energy, as shown in Fig. 11 (a), which also effectively restricted the growth of α-Al dendrites by impeding the diffusion of Al atoms onto the growing crystals and prevented the coalescence of dendrites at the end of α-Al solidification [28]. The significant grain refinement in our work could also be observed clearly from the electron backscatter diffraction (EBSD) analysis shown in Fig. 10 (b and c). Additionally, many submicron-sized TiB_2 particles would be engulfed by the α-Al grains by the advancing S/L interface, as shown in Fig. 11 (b and c). The corresponding SAED pattern and HRTEM micrograph of area A in Fig. 11 (c) were further shown separately in Fig. 11 (d) and (e). As observed, the interface between the TiB_2 particles and the matrix was very clean. At the end of solidification, the final spatial configuration of the TiB_2 particles formed as illustrated in Fig. 11 (f).

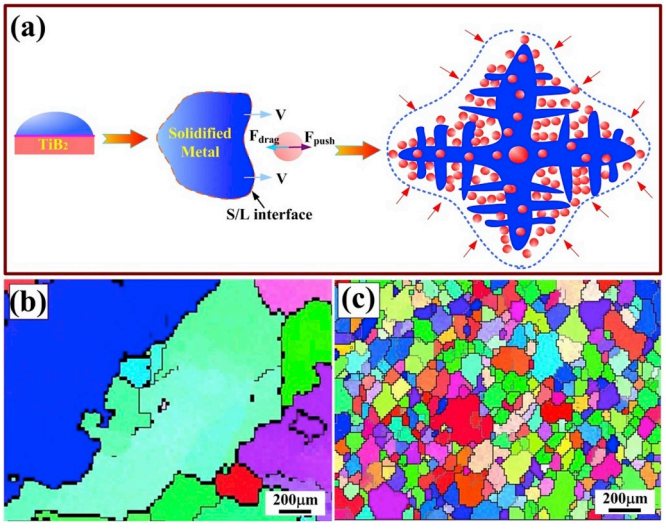

Fig. 10. (a) Schematic illustration of the effects of bimodal-sized TiB_2 particles during solidification. EBSD analysis of Al–7Si–4Cu alloys without and with TiB_2 particle addition: (b) BS-0.0 and (c) and BS-1.0.

It is well known that Si has a low solid solubility in an Al matrix (the maximum of 1.65% at 577 °C [43]), which indicates that most Si solutes are rejected by the growing α-Al dendrites and lead to the coarse eutectic Si structure at the interdendritic regions, as shown in Fig. 5 (a). In other words, the available growth of the eutectic Si structure was restricted to the left space after the α-Al dendrite skeleton formed. Hence, the finer and equiaxed α-Al grains in the inoculated alloys facilitated the refinement and homogeneous distribution of eutectic Si due to the presence of more tortuous boundaries. Furthermore, the high concentrations of nanosized TiB_2 particles pushed ahead of the equiaxed solidification front interacted with both the growing eutectic Si and eutectic Al and thus restricted solute redistribution between them, which also caused the refinement of eutectic Al–Si structure [18].

4.2. Mechanical property enhancement mechanisms

In our work, the yield strength of Al–7Si–4Cu alloys was significantly enhanced with the bimodal-sized TiB_2 particle addition. The relevant strengthening mechanisms are mainly involved in grain-refinement strengthening, Orowan strengthening, and thermal-mismatch strengthening [14], as schematically illustrated in Fig. 12. To figure out the contributions of every strengthening mechanism, the BS-0.1 and BS-0.7 alloys were deliberately chosen for theoretical analyses.

In our work, the grain sizes of primary α-Al dendrites greatly decreased in the presence of bimodal-sized TiB_2 particles compared to those in the base alloy, as observed from Fig. 4. Accordingly, the resultant increase in grain boundary density improved the yield strength to some extent. The relationship between the grain size and the yield strength was well described by the classical Hall-Petch relationship, as follows [14]:

$$\Delta\sigma_{HP} = k\left(d^{-\frac{1}{2}} - d_0^{-\frac{1}{2}}\right) \tag{2}$$

where k (74.0 $\mu m^{1/2}$[14]) is the Hall-Petch slope, and d and d_0 are the average grain sizes of the base alloy and the alloys with TiB_2 addition. According to equation (2), the grain refinement contributed only 1.7 MPa and 2.6 MPa to the yield strength of the BS-0.1 and BS-0.7 alloys, respectively.

Due to the difference in the thermal expansion coefficient between the TiB_2 particles (7.8×10^{-6} K^{-1}) [26] and the matrix (23.6×10^{-6} K^{-1}) [14], a large density of geometrically necessary dislocations would be generated in the vicinity of the TiB_2 particles during water quenching immediately after solution heat treatment. The interaction between the TiB_2 particles and these dislocations played an important role in the increase in yield strength, which was quantitatively determined as follows [14]:

$$\Delta\sigma_{CTE} = \eta G b \rho^{\frac{1}{2}} \tag{3}$$

$$\rho = \frac{12\Delta\alpha\,\Delta T\,V_P}{bD(1-V_P)} \tag{3a}$$

where G is the shear modulus (26.2 GPa [14]), b is the Burgers vector of the matrix (0.286 nm [14]), V_p and D are the volume fraction and average diameter of the reinforcements (78.2 nm), η is a constant of approximately 1.25 [14], $\Delta\alpha$is the difference in the coefficient of

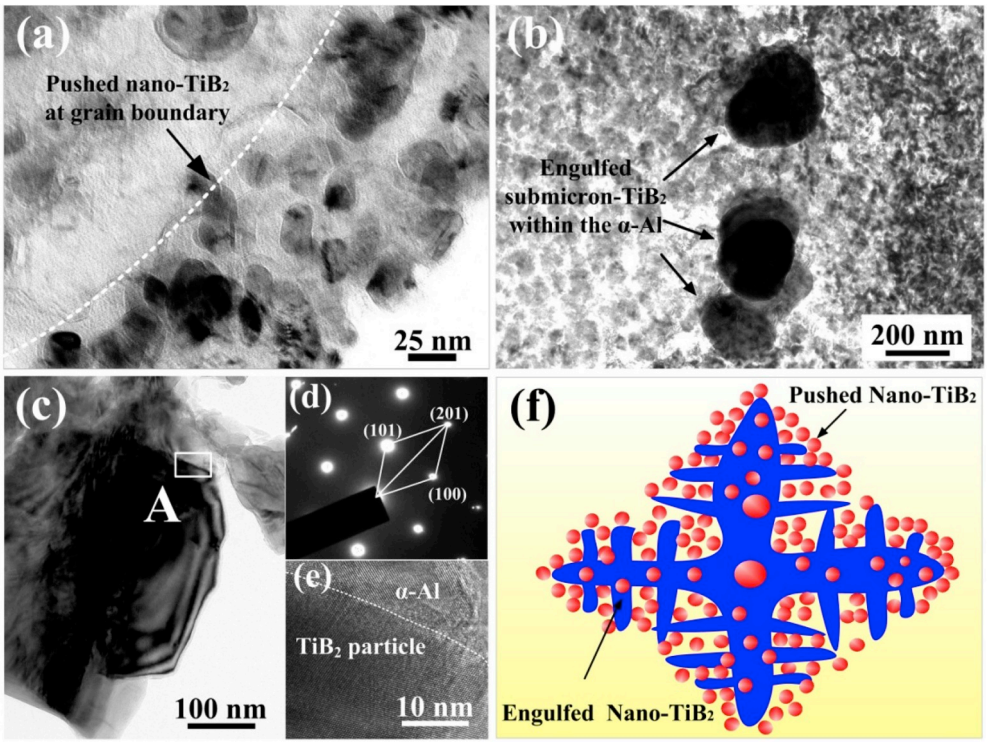

Fig. 11. TEM micrographs showing the distribution of (a) the nanosized TiB_2 particles in BS-0.7 along the grain boundaries; (b) and (c) submicron-sized TiB_2 particle within the α-Al; (d) and (e) the corresponding SAED pattern and HRTEM micrograph of the submicron-sized TiB_2 particle in area A. (f) Schematic illustration of the spatial configuration of TiB_2 particles.

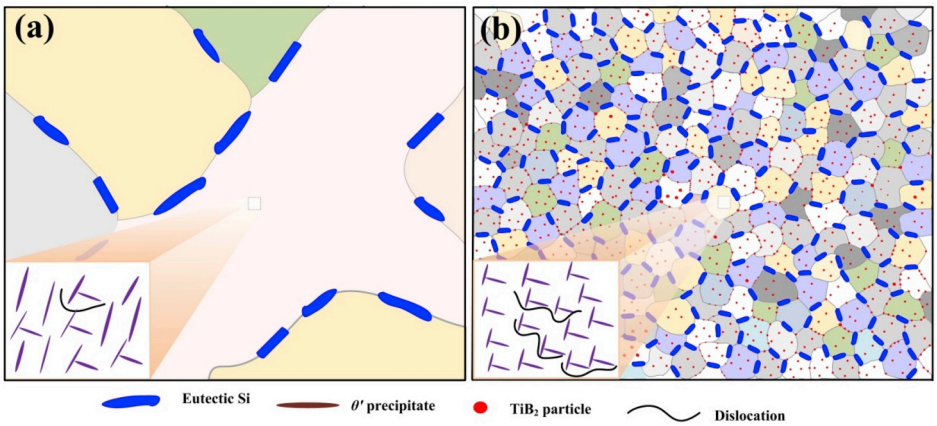

Fig. 12. (a) Schematic illustration of the strengthening and toughening effects of bimodal-sized TiB_2 particles on Al–7Si–4Cu alloys during deformation.

thermal expansion (CTE) between the Al matrix and reinforcements; and ΔT (510 °C) represents the difference between the processing temperature and the mold temperature. According to equations (3) and (3a), the increased dislocation density contributed 15.1 MPa and 39.9 MPa to the yield strength of the BS-0.1 and BS-0.7 alloys, respectively.

Furthermore, according to the Orowan strengthening effect [29], the bimodal-sized reinforcement (<1 μm) made a crucial contribution to the significant improvement in yield strength. In our work, the small TiB_2 particles pinned down the dislocations and thereby strengthening the alloys, as described by equation (4) [14].

$$\Delta\sigma_{TiB_2} = \frac{0.13Gb}{D\left[(2V_P)^{-\frac{1}{3}} - 1\right]} \ln\frac{D}{2b} \tag{4}$$

According to equation (4), the Orowan strengthening effect by TiB_2 particles contributed 7.3 MPa and 15.6 MPa to the yield strength of the BS-0.1 and BS-0.7 alloys, respectively.

In addition, as shown in Fig. 6 (a and b), the average diameter of the plate-like θ' precipitates was refined from 52 nm to 42 nm and 35 nm; meanwhile, the density was also enhanced. It has been reported that second phase particles could greatly affect the aging kinetics of the precipitates [6,44]. In the existence of TiB_2 particles in our work, the enhanced dislocations around the TiB_2 ceramic particles due to the difference in the CTE promoted the segregation of elemental Cu and then acted as the nucleation sites for θ' precipitates during aging [44]. Thus, a finer and more uniform θ' phase precipitated out. The finer θ' precipitates could strongly impede the moving dislocations during deformation, which led to the increased yield strength in terms of precipitation strengthening, as described by the modified Orowan

equation [45]:

$$\Delta\sigma_{\theta'} = \frac{MGb}{2\pi\sqrt{1-\upsilon}}\left(\frac{1}{1.123d\sqrt{\frac{0.318\pi}{af}} - \frac{\pi d}{8} - \frac{1.061d}{a}}\right)\ln\frac{0.981d}{ab} \quad (5)$$

where M, υ, f and a represent the Taylor factor for Al (approximately equal to 3 [44]), Poisson's ratio (1/3 for Al [44]), the volume fraction and the aspect ratio of the θ' precipitates ($a = d/t$, where t and d are the thickness and diameter of the precipitates), respectively. According to Ref. [46], f was estimated to be 4.5% for this work. By substituting the values of M, υ, f, a, d and t into equation (5), it was found that the contributions from the θ' phase in BS-0.1 and BS-0.7 alloys are 26.2 MPa and 50.8 MPa higher than that in the base alloy, respectively.

In conclusion, the yield strength (σ_T) of Al–7Si–4Cu alloy with 0.7% bimodal-sized TiB_2 particle addition could be predicted as follows [14]:

$$\sigma_T = \sigma_0 + \Delta\sigma_{HP} + \left[\left(\Delta\sigma_{Orwan}\right)^2 + \left(\Delta\sigma_{CTE}\right)^2\right]^{1/2} \quad (6)$$

According to equation (6), the introduction of 0.1% and 0.7% bimodal-sized TiB_2 particles theoretically contributed 38.3 MPa and 79.6 MPa to the yield strength of the Al–7Si–4Cu alloy, which agrees well with the actual values, as shown in Table 2. Based on the theoretical analysis above, the significant improvement in the yield strength of the inoculated alloys could be primarily attributed to the thermal-mismatch strengthening, θ' precipitation strengthening and Orowan strengthening effects by the bimodal-sized TiB_2 particles. Moreover, grain-refinement strengthening effect also partly accounted for this improvement.

In our work, the ductility of the Al–7Si–4Cu alloy inoculated by 0.7% bimodal-sized TiB_2 particles was also greatly improved by 71.1%, when compared to that of the base alloy. It is well known that the improved ductility of Al–Si alloys was mainly attributable to three possible mechanisms: gain refinement of α-Al dendrites, eutectic Si refinement and the introduction of in situ bimodal-sized TiB_2 particles [47,48]. With the addition of 0.7% TiB_2 particles, the coarse grain structure in the base alloy was transformed into much finer equiaxed crystals, a reduction of 79.0%. Generally, the significantly refined α-Al grain structure could suppress the crack initiation and propagation because the cracking path was much more tortuous with the remarkable increase of the density of grain boundaries [6]. Moreover, according to previous studies [48,49], the relationship between uniform elongation ($\overline{e_F}$) of the Al–Si alloys and the average particle size of eutectic Si ($\overline{d_{Si}}$) could be described by a lognormal relationship, as follows:

$$\overline{e_F} = \alpha\cdot\left(\overline{d_{Si}}\right)^{\beta}\ (\alpha>,\ \beta<0)$$

It is well acknowledged that the long needle-shaped eutectic Si structure, as the crack source site, is more prone to cracking. With the addition of 0.7% in situ bimodal-sized TiB_2 particles, in our work, the coarse eutectic Si structure was significantly refined by 53.7%. As a result, the stress concentrations around eutectic Si were greatly reduced during plastic deformation and crack initiation became more difficult. Furthermore, it is worth mentioning that the particle size of the added TiB_2 was a mixture of nano- and submicron-sized TiB_2 particles. Unlike their micron-sized counterparts, these small particles were much more impossible to cause stress concentrations. In addition, according to a recent study [47], the nanosized TiB_2 particles with uniform distribution along the grain boundaries could also effectively constrain crack propagation and lead to crack branching or deflection in different directions during deformation.

5. Conclusions

(1) Bimodal-sized TiB_2 particles were in situ synthesized in an Al–Ti–B system, wherein no brittle Al_3Ti compound was found. The size distribution of synthesized TiB_2 particles ranged from less than 100 nm to 350 nm.

(2) The bimodal-sized TiB_2 particles could effectively refine the primary α-Al dendrites and eutectic Si by 79.0% and 53.7%, respectively, which was far beyond the efficiency and ability of the micron-sized TiB_2 particles. The added bimodal-sized TiB_2 particles were highly potent at promoting the heterogeneous nucleation of α-Al crystals at a lower undercooling. Meanwhile, the finer primary α-Al dendrites also led to the refinement of the Al–Si eutectic due to the reduction in growing space. Additionally, the θ' precipitates was also greatly refined by 32.7%.

(3) The strength and ductility of Al–7Si–4Cu alloys were simultaneously enhanced with in situ bimodal-sized TiB_2 particle addition. At 0.7% bimodal-sized TiB_2 addition, the yield strength, ultimate tensile strength and elongation to fracture of the Al–7Si–4Cu alloy were significantly enhanced by 26.3%, 17.4% and 71.1% over those of the base alloy, respectively. The increased strength could be primarily ascribed to the thermal-mismatch strengthening, θ' precipitation strengthening and the Orowan strengthening effects by bimodal-sized TiB_2 particles. Moreover, the grain-refinement strengthening effect also partly accounted for this improvement. The significant refinement of the α-Al dendrites and eutectic Si and the small size of the bimodal-sized TiB_2 particles may effectively account for the excellent elongation.

Author contributions section

Qiang Li: Writing-original draft, Methodology, Formal analysis. Feng Qiu: Conceptualization, Supervision, Resources, Funding acquisition, Project administration. Bai-Xin Dong: Supervision, Validation, Investigation. Xiang Gao: Writing-review&editing, Resources, Methodology, Formal analysis. Shi-Li Shu: Writing-review & editing, Data curation, Formal analysis. Hong-Yu Yang: Writing-review&editing, Supervision, Data curation. Qi-Chuan Jiang: Conceptualization, Resources, Funding acquisition, Project administration.

Declaration of competing interest

The authors declare that they have no known competing financial interests or personal relationships that could have appeared to influence the work reported in this paper.

Acknowledgements

This work is supported by the National Natural Science Foundation of China (NNSFC, No. 51971101 and No. 51771081), the Science and Technology Development Program of Jilin Province, China (20190302004GX), and the Source Innovation Plan of Qingdao City, China (No. 18-2-2-1-jch).

References

[1] M.W. Liu, R.X. Zheng, W.L. Xiao, X.H. Yu, Q.M. Peng, C.L. Ma, Concurrent enhancement of strength and ductility for Al-Si binary alloy by refining Si phase to nanoscale, Mater. Sci. Eng., A 751 (2019) 303–310.

[2] K.Q. Hu, X. Ma, T. Gao, Q.F. Xu, Z. Qian, Y.Y. Wu, X.F. Liu, Morphological transformation mechanism of eutectic Si phases in Al-Si alloys by nano-AlN_p, J. Alloys Compd. 765 (2018) 113–120.

[3] Y.C. Tzeng, S.Y. Jian, Effects of the addition of trace amounts of Sc on the microstructure and mechanical properties of Al-11.6Si alloys, Mater. Sci. Eng., A 723 (2018) 22–28.

[4] Y. Zhang, H.L. Zheng, Y. Liu, L. Shi, R.F. Xu, X.L. Tian, Cluster-assisted nucleation of silicon phase in hypoeutectic Al-Si alloy with further inoculation, Acta Mater. 70 (2014) 162–173.

[5] X. Zhang, L.K. Huang, B. Zhang, Y.Z. Chen, S.Y. Duan, G. Liu, C.L. Yang, F. Liu, Enhanced strength and ductility of A356 alloy due to composite effect of near-rapid solidification and thermo-mechanical treatment, Mater. Sci. Eng., A 753 (2019) 168–178.

[6] W.S. Tian, Q.L. Zhao, Q.Q. Zhang, F. Qiu, Q.C. Jiang, Simultaneously increasing the high-temperature tensile strength and ductility of nano-sized TiC_p reinforced Al-Cu matrix composites, Mater. Sci. Eng., A 717 (2018) 105–112.

[7] B. Chen, S.K. Moon, X. Yao, G. Bi, J. Shen, J. Umeda, K. Kondoh, Strength and strain hardening of a selective laser melted AlSi10Mg alloy, Scripta Mater. 141 (2017) 45–49.

[8] M.D. Giovanni, J.M. Warnett, M.A. Williams, P. Srirangam, 3D imaging and quantification of porosity and intermetallic particles in strontium modified Al-Si alloys, J. Alloys Compd. 727 (2017) 353–361.

[9] M. Colombo, E. Gariboldi, A. Morri, Er addition to Al-Si-Mg-based casting alloy: effects on microstructure, room and high temperature mechanical properties, J. Alloys Compd. 708 (2017) 1234–1244.

[10] D.F. Li, C.X. Cui, X. Wang, Q.Z. Wang, C. Chen, S.Q. Liu, Microstructure evolution and enhanced mechanical properties of eutectic Al-Si die cast alloy by combined alloying Mg and La, Mater. Des. 90 (2016) 820–828.

[11] Z. Lu, L.J. Zhang, Thermodynamic description of the quaternary Al-Si-Mg-Sc system and its application to the design of novel Sc-additional A356 alloys, Mater. Des. 116 (2017) 427–437.

[12] P. Pandee, C.M. Gourlay, S.A. Belyakov, U. Patakham, G. Zeng, C. Limmaneevichitr, $AlSi_2Sc_2$ intermetallic formation in Al-7Si-0.3Mg-xSc alloys and their effects on as-cast properties, J. Alloys Compd. 731 (2018) 1159–1170.

[13] G. Wang, Q. Wang, M.A. Easton, M.S. Dargusch, M. Qian, D.G. Eskin, D.H. StJohn, Role of ultrasonic treatment, inoculation and solute in the grain refinement of commercial purity aluminium, Sci. Rep. 7 (2017) 9729.

[14] Q. Li, F. Qiu, Y.Y. Gao, B.X. Dong, S.L. Shu, M.M. Lv, H.Y. Yang, Q.L. Zhao, Q. C. Jiang, Microstructure refinement and strengthening mechanisms of bimodal-sized and dual-phased (TiC_n-Al_3Ti_m)/Al hybrid composites assisted ultrasonic vibration, J. Alloys Compd. 788 (2019) 1309–1321.

[15] T.E. Quested, Understanding mechanisms of grain refinement of aluminium alloys by inoculation, Mater. Sci. Technol. 20 (2004) 1357–1369.

[16] H.X. Jiang, Q. Sun, L.L. Zhang, J.Z. Zhao, Al-Ti-C master alloy with nano-sized TiC particles dispersed in the matrix prepared by using carbon nanotubes as C source, J. Alloys Compd. 748 (2018) 774–782.

[17] A.L. Greer, Overview: application of heterogeneous nucleation in grain-refining of metals, J. Chem. Phys. 145 (2016) 211704.

[18] P.L. Schaffer, L. Arnberg, A.K. Dahle, Segregation of particles and its influence on the morphology of the eutectic silicon phase in Al-7 wt% Si alloys, Scripta Mater. 54 (2006) 677–682.

[19] D. Qiu, J.A. Taylor, M.X. Zhang, P.M. Kelly, A mechanism for the poisoning effect of silicon on the grain refinement of Al-Si alloys, Acta Mater. 55 (2007) 1447–1456.

[20] A.L. Greer, P.S. Cooper, M.W. Meredith, W. Schneider, P. Schumacher, J.A. Spittle, A. Tronche, Grain refinement of aluminium alloys by inoculation, Adv. Eng. Mater. 5 (2003) 81–91.

[21] S.L. Pramod, Ravikirana, A.K.P. Rao, B.S. Murty, S.R. Bakshi, Microstructure and mechanical properties of as-cast and T6 treated Sc modified A356-5TiB_2 in-situ composite, Mater. Sci. Eng., A 739 (2019) 383–394.

[22] S.X. Ji, F. Amirkhanlub, A. Mostaedc, d R. Beanland, Atomic structure and interface chemistry in a high-stiffness and high-strength Al-Si-Mg/TiB_2 nanocomposite, Mater. Sci. Eng., A 763 (2019) 138072.

[23] T.M. Wang, Y.F. Zhao, Z.N. Chen, Y.P. Zheng, H.J. Kang, Combining effects of TiB_2 and La on the aging behavior of A356 alloy, Mater. Sci. Eng., A 644 (2015) 425–430.

[24] M.L. Wang, D. Chen, Z. Chen, Y. Wu, F.F. Wang, N.H. Ma, H.W. Wang, Mechanical properties of in-situ TiB_2/A356 composites, Mater. Sci. Eng., A 590 (2014) 246–254.

[25] B. Dang, X. Zhang, Y.Z. Chen, C.X. Chen, H.T. Wang, F. Liu, Breaking through the strength-ductility trade-off dilemma in an Al-Si-based casting alloy, Sci. Rep. 6 (2016) 30874.

[26] H. Li, X.M. Wang, L.H. Chai, H.J. Wang, Z.Y. Chen, Z.L. Xiang, T.N. Jin, Microstructure and mechanical properties of an in-situ TiB_2/Al-Zn-Mg-Cu-Zr composite fabricated by Melt-SHS process, Mater. Sci. Eng., A 720 (2018) 60–68.

[27] L.Y. Chen, J.Q. Xu, H. Choi, H. Konishi, S. Jin, X.C. Li, Rapid control of phase growth by nanoparticles, Nat. Commun. 5 (2014) 3879–4879.

[28] K. Wang, H.Y. Jiang, Y.W. Jia, H. Zhou, Q.D. Wang, B. Ye, W.J. Ding, Nanoparticle-inhibited growth of primary aluminum in Al-10Si alloys, Acta Mater. 103 (2016) 252–263.

[29] X.P. Li, G. Ji, Z. Chen, A. Addad, Y. Wu, H.W. Wang, J. Vleugels, J.V. Humbeeck, J. P. Kruth, Selective laser melting of nano-TiB_2 decorated AlSi10Mg alloy with high fracture strength and ductility, Acta Mater. 129 (2017) 183–193.

[30] M.K. Akbari, K. Shirvanimoghaddam, Z.Y. Hai, S. Zhuiykov, H. Khayyam, Al-TiB_2 micro/nanocomposites: particle capture investigations, strengthening mechanisms and mathematical modelling of mechanical properties, Mater. Sci. Eng., A 682 (2017) 98–106.

[31] W.S. Tian, Q.L. Zhao, Q.Q. Zhang, F. Qiu, Q.C. Jiang, Enhanced strength and ductility at room and elevated temperatures of Al-Cu alloy matrix composites reinforced with bimodal-sized TiC_p compared with monomodal-sized TiC_p, Mater. Sci. Eng., A 724 (2018) 368–375.

[32] R.T. Mousavian, R.A. Khosroshahi, S. Yazdani, D. Brabazon, A.F. Boostani, Fabrication of aluminum matrix composites reinforced with nano- to micrometer-sized SiC particles, Mater. Des. 89 (2016) 58–70.

[33] H. Men, B. Jiang, Z. Fan, Mechanisms of grain refinement by intensive shearing of AZ91 alloy melt, Acta Mater. 58 (2010) 6526–6534.

[34] K. Kim, B.C. Zhou, C. Wolverton, Interfacial stability of θ′/Al in Al-Cu alloys, Scripta Mater. 159 (2019) 99–103.

[35] I. Aguilera-Luna, M.J. Castro-Román, J.C. Escobedo-Bocardo, F.A. García-Pastor, M. Herrera-Trejo, Effect of cooling rate and Mg content on the Al-Si eutectic for Al-Si-Cu-Mg alloys, Mater. Char. 95 (2014) 211–218.

[36] L. Bolzoni, N.H. Babu, Engineering the heterogeneous nuclei in Al-Si alloys for solidification control, Appl. Mater. Today 5 (2016) 255–259.

[37] M.X. Zhang, P.M. Kelly, M.A. Easton, J.A. Taylor, Crystallographic study of grain refinement in aluminum alloys using the edge-to-edge matching model, Acta Mater. 53 (2005) 1427–1438.

[38] B. Bramfitt, The effect of carbide and nitride additions on the heterogeneous nucleation behavior of liquid iron, Metall. Trans. 1 (1970) 1987–1995.

[39] Z. Fan, Y. Wang, Y. Zhang, T. Qin, X.R. Zhou, G.E. Thompson, T. Pennycook, T. Hashimoto, Grain refining mechanism in the Al/Al-Ti-B system, Acta Mater. 84 (2015) 292–304.

[40] M. Easton, D. StJohn, An analysis of the relationship between grain size, solute content, and the potency and number density of nucleant particles, Metall. Trans. A 36 (2005) 1911–1920.

[41] A.L. Greer, J. Worth, P.V. Evans, M.A. Kearns, P. Fisher, A.H. Green, New studies of nucleation mechanisms in aluminium alloys: implications for grain refinement practice, Mater. Sci. Technol. 14 (1998) 394–404.

[42] A.L. Greer, A.M. Bunn, A. Tronche, P.V. Evans, D.J. Bristow, Modelling of inoculation of metallic melts: application to grain refinement of aluminium by Al-Ti-B, Acta Mater. 48 (2000) 2823–2835.

[43] J.L. Murray, A.J. McAlister, The Al-Si (aluminum-silicon) system, Bull. Alloy Phase Diagr. 5 (1984) 74–84.

[44] H.B. Yang, T. Gao, H.N. Zhang, J.F. Nie, X.F. Liu, Enhanced age-hardening behavior in Al-Cu alloys induced by in-situ synthesized TiC nanoparticles, J. Mater. Sci. Technol. 35 (2019) 374–382.

[45] W.S. Tian, Q.L. Zhao, Q.Q. Zhang, F. Qiu, Q.C. Jiang, Simultaneously increasing the high-temperature tensile strength and ductility of nano-sized TiC_p reinforced Al-Cu matrix composites, Mater. Sci. Eng., A 717 (2018) 105–112.

[46] X.Q. Zhao, M.J. Shi, J.H. Chen, S.B. Wang, C.H. Liu, C.L. Wu, A facile electron microscopy method for measuring precipitate volume fractions in AlCuMg alloys, Mater. Char. 69 (2012) 31–36.

[47] X.P. Li, G. Ji, Z. Chen, A. Addad, Y. Wu, H.W. Wang, J. Vleugels, J. Van Humbeeck, J.P. Kruth, Selective laser melting of nano-TiB_2 decorated AlSi10Mg alloy with high fracture strength and ductility, Acta Mater. 129 (2017) 183–193.

[48] C. Xu, C.L. Ma, Y.F. Sun, S. Hanada, G.X. Lu, S.K. Guan, Optimizing strength and ductility of Al-7Si-0.4Mg foundry alloy: role of Cu and Sc addition, J. Alloys Compd. 810 (2019) 151944.

[49] N.D. Alexopoulos, M. Tiryakioğlu, A.N. Vasilakos, S.K. Kourkoulis, The effect of Cu, Ag, Sm and Sr additions on the statistical distributions of Si particles and tensile properties in A357-T6 alloy castings, Mater. Sci. Eng., A 604 (2014) 40–45.